

Exploring copper(i)-based dye-sensitized solar cells: a complementary experimental and TD-DFT investigation†

Biljana Bozic-Weber,^a Valerie Chaurin,^a Edwin C. Constable,^{*a} Catherine E. Housecroft,^{*a} Markus Meuwly,^{*b} Markus Neuburger,^a Jennifer A. Rudd,^a Ewald Schönhofer^a and Liselotte Siegfried^a

Received 30th May 2012, Accepted 12th September 2012

DOI: 10.1039/c2dt31159c

The structures and properties of the homoleptic copper(i) complexes $[\text{Cu}(\mathbf{1})_2][\text{PF}_6]$ and $[\text{Cu}(\mathbf{2})_2][\text{PF}_6]$ ($\mathbf{1}$ = 6,6'-dimethyl-2,2'-bipyridine, $\mathbf{2}$ = 6,6'-bis{2-[4-(*N,N'*-diphenylamino)phenyl]ethenyl}-2,2'-bipyridine) are compared, and a strategy of ligand exchange in solution has been used to prepare eight TiO_2 surface-bound heteroleptic complexes incorporating ligands with bpy metal-binding domains and carboxylate or phosphonate anchoring groups. The presence of the extended π -system in $\mathbf{2}$ significantly improves dye performance, and the most efficient sensitizers are those with phosphonate or phenyl-4-carboxylate anchoring units; a combination of $[\text{Cu}(\mathbf{2})_2]^+$ with the phosphonate anchoring ligand gives a very promising performance ($\eta = 2.35\%$ compared to 7.29% for standard dye N719 under the same conditions). The high-energy bands in the electronic absorption spectrum of $[\text{Cu}(\mathbf{2})_2]^+$ which arise from ligand-based transitions dominate the spectrum, whereas that of $[\text{Cu}(\mathbf{1})_2]^+$ exhibits both MLCT and ligand $\pi^* \leftarrow \pi$ bands. Both $[\text{Cu}(\mathbf{1})_2][\text{PF}_6]$ and $[\text{Cu}(\mathbf{2})_2][\text{PF}_6]$ are redox active; while the former exhibits both copper-centred and ligand-based processes, $[\text{Cu}(\mathbf{2})_2][\text{PF}_6]$ shows only ligand-based reductions. Results of TD-DFT calculations support these experimental data. They predict an electronic absorption spectrum for $[\text{Cu}(\mathbf{1})_2]^+$ with an MLCT band and high-energy ligand-based transitions, and a spectrum for $[\text{Cu}(\mathbf{2})_2]^+$ comprising transitions involving mainly contributions from orbitals with ligand $\mathbf{2}$ character. We have assessed the effects of the atomic orbital basis set on the calculated absorption spectrum of $[\text{Cu}(\mathbf{1})_2]^+$ and show that a realistic spectrum is obtained by using a 6-311++G** basis set on all atoms, or 6-311++G** on copper and 6-31G* basis set on all other atoms; a smaller basis set on copper leads to unsatisfactory results. Electronic absorption spectra of six heteroleptic complexes have been predicted using TD-DFT calculations, and the transitions making up the dominant bands analysed in terms of the character of the HOMO–LUMO manifold. The calculational data reveal dominant phosphonate ligand character in the LUMO for the dye found to function most efficiently in practice, and also reveal that the orbital character in the HOMOs of the two most efficient dyes is dominated by the non-anchoring ligand $\mathbf{2}$, suggesting that ligand $\mathbf{2}$ enhances the performance of the sensitizer by minimizing back-migration of an electron from the semiconductor to the dye.

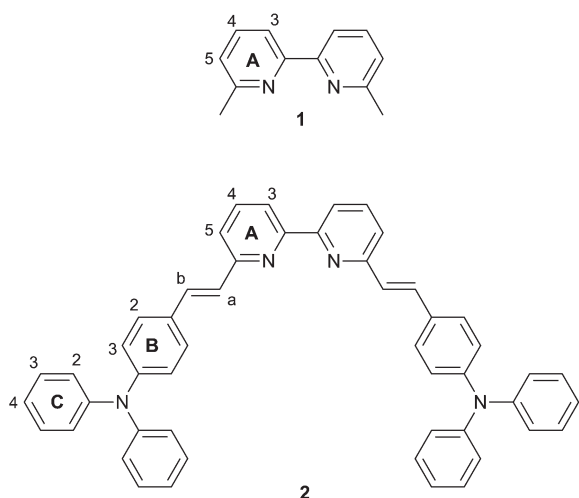
Introduction

We are currently investigating the application of complexes containing Earth-abundant metals in dye-sensitized solar cells (DSCs). Within this remit, the photophysical properties of d^{10} metal complexes,¹ and copper(i)-based² DSCs appear particularly promising.^{3–14} The lability of copper(i) complexes^{15,16} has led us to develop a strategy for the assembly of heteroleptic complexes directly on a TiO_2 semiconductor surface. An oligopyridine ligand, L' , containing anchoring substituents (*e.g.* CO_2H or $\text{PO}(\text{OH})_2$) is bound to a titania nanoparticle surface and the modified surface is subsequently exposed to a solution of a homoleptic $[\text{CuL}_2]^+$ complex. Over a period of one or more days, ligand exchange occurs to give surface-anchored $[\text{CuLL}]^+$ complexes.¹² This method allows us to screen relatively large numbers of complexes without it being necessary to isolate the

^aDepartment of Chemistry, University of Basel, Spitalstrasse 51, CH-4056 Basel, Switzerland. E-mail: catherine.housecroft@unibas.ch, edwin.constable@unibas.ch; Fax: +41 61 267 1018; Tel: +41 61 267 1008

^bDepartment of Chemistry, University of Basel, Klingelbergstrasse 80, CH-4056 Basel, Switzerland

†Electronic supplementary information (ESI) available: Table S1: comparison of DFT and single crystal X-ray structural parameters for $[\text{Cu}(\mathbf{1})_2]^+$ and $[\text{Cu}(\mathbf{2})_2]^+$; Tables S2 and S3: orbital contributions to electronic absorption transitions; Fig. S1 and S5: transitions making up calculated absorption bands in $[\text{Cu}(\mathbf{2})\text{L}]^+$ ($L = \mathbf{2}$ – $\mathbf{5}$); Fig. S2–S4, S6–S8: compositions of HOMOs and LUMOs of $[\text{Cu}(\mathbf{1})_2]^+$, $[\text{Cu}(\mathbf{1})\text{L}]^+$ and $[\text{Cu}(\mathbf{2})\text{L}]^+$ ($L = \mathbf{3}$ – $\mathbf{5}$). CCDC 885553–885556. For ESI and crystallographic data in CIF or other electronic format see DOI: 10.1039/c2dt31159c



Scheme 1 Ligand structures **1** and **2**, and labelling for ^1H NMR spectroscopic assignments.

heteroleptic species (which is often not possible because of the rapid establishment of statistical solution equilibria between homo- and heteroleptic species) and to study the effects of a wide range of substituents on the efficiencies of photosensitisers. To aid in the design of new and more efficient copper(i) complexes for DSCs, Lu *et al.* have recently demonstrated the use of DFT and TD-DFT quantum chemical methods for the investigation of the molecular and electronic structures and optical absorption spectra of homoleptic $[\text{CuL}_2]^+$ and $[\text{CuL}_2][\text{PF}_6]$ ($\text{L} = 6,6'$ -dimethyl-2,2'-bipyridine-4,4'-dimethylformate) and related heteroleptic complexes both in the gas phase and MeCN solution.^{17,18} In order to evaluate the validity of such theoretical data, comparisons with experimental data are critical. Here we present a complementary experimental and theoretical investigation of the homoleptic copper(i) complexes $[\text{Cu}(\mathbf{1})_2]^+$ and $[\text{Cu}(\mathbf{2})_2]^+$ (see Scheme 1 for ligands **1** and **2**). These complexes have been used to prepare eight TiO_2 surface-bound heteroleptic complexes incorporating carboxylate or phosphonate anchoring groups and their efficiencies as dyes in DSCs have been measured. TD-DFT calculations have also been carried out on six of the heteroleptic complexes. The archetype complex $[\text{Cu}(\mathbf{1})_2][\text{PF}_6]$ was selected because the $[\text{Cu}(\mathbf{1})_2]^+$ cation^{19–25} is structurally simple and its electrochemical and photophysical properties are well established. The presence of substituents at the 6- and 6'-positions in 2,2'-bipyridine ligands renders the copper(i) complexes stable with respect to aerial oxidation.²⁶ On moving from ligand **1** to **2**, the π -conjugation is significantly extended and the size of the complex increased, and we were interested in investigating what effects these factors would have upon the efficiency of the DSCs into which it is incorporated. In addition, **2** has the potential for subsequent facile functionalization at the *N,N*-diphenylamino substituent.

Experimental

^1H and ^{13}C NMR spectra were measured on a Bruker DRX-500 MHz NMR spectrometer; chemical shifts are

referenced to residual solvent peaks with TMS = δ 0 ppm. Electronic absorption and emission spectra were recorded using an Agilent 8453 spectrophotometer and Shimadzu RF-5301 PC spectrofluorometer, respectively. Solution lifetime measurements were made using an Edinburgh Instruments mini- τ apparatus equipped with an Edinburgh Instruments EPLED-300 picosecond pulsed diode laser ($\lambda_{\text{ex}} = 467$ or 404 nm, pulse width = 75.5 or 48.2 ps, respectively) with the appropriate wavelength filter. The quantum yields were measured with an absolute PL quantum yield spectrometer C11347 Quantaurus_QY from Hamamatsu. Solid state electronic absorption spectra of Cu(i)-containing dyes on TiO_2 were measured using a Varian Cary 5000 with a conducting glass with a TiO_2 layer as a blank. Electrospray and MALDI-TOF mass spectra were recorded on either a Bruker esquire 3000plus or PerSeptive Biosystems Voyager instrument, respectively. Electrochemical data were recorded using a CH Instruments potentiostat (model 900B) with glassy carbon working and platinum auxiliary electrodes; a silver wire was used as a pseudo-reference electrode. Solvents for the electrochemistry were dry and purified, and the supporting electrolyte was 0.1 M $[\text{Bu}_4\text{N}][\text{PF}_6]$; an external reference of Cp_2Fe was measured at the start and again at the end of each experiment.

6,6'-Dimethyl-2,2'-bipyridine (**1**) and 4-(*N,N*-diphenylamino)-benzaldehyde were purchased from Sigma Aldrich. $[\text{Cu}(\text{MeCN})_4][\text{PF}_6]$ was prepared according to the literature procedure²⁷ and the synthesis of 6,6'-bis(diethylphosphonomethyl)-2,2'-bipyridine was based on that reported by Mukkala²⁸ replacing 6,6'-bis(bromomethyl)-2,2'-bipyridine by 6,6'-bis(chloromethyl)-2,2'-bipyridine. Compounds **3**,⁶ **4**,²⁹ **5**³⁰ and **6**³⁰ were prepared as previously described.

Ligand 2: method 1

Compound **1** (550 mg, 2.98 mmol) and 4-(*N,N*-diphenylamino)-benzaldehyde (1.87 g, 6.87 mmol) were stirred in dry DMF (70 cm^3) in a reaction flask and KO^tBu (1.005 g, 8.96 mmol) was added. The vessel was flushed with N_2 for 10 min and the reaction mixture was stirred for 56 h in the dark after which time a dark yellow solid precipitated. This was filtered and dried in air. The crude product was dissolved in the minimum amount of CH_2Cl_2 and purified by column chromatography (SiO_2 , CH_2Cl_2). The first (orange) fraction was collected and solvent was removed *in vacuo*. Compound **2** was isolated as a yellow powder (1.13 g, 1.63 mmol, 54.7%). ^1H NMR (500 MHz, CDCl_3) δ /ppm 8.40 (dd, 7.8, 0.6 Hz 2H, H^{A3}), 7.80 (t, $J = 7.8$ Hz, 2H, H^{A4}), 7.72 (d, $J = 16.0$ Hz, 2H, H^{b}), 7.47 (d_{AB} , $J = 8.6$ Hz, 2H, H^{B2}), 7.37 (dd, $J = 7.7$, 0.6 Hz, 2H, H^{A5}), 7.26 (m, 4H, H^{C3}), 7.13 (m, 10H, $\text{H}^{\text{C2+a}}$), 7.05 (m, 8H, $\text{H}^{\text{C4+B3}}$). ^{13}C NMR (126 MHz, CDCl_3) δ /ppm 156.1 (C^{A2}), 155.3 (C^{A6}), 148.1 (C^{B4}), 147.6 (C^{C1}), 137.4 (H^{A4}), 132.4 (C^{b}), 130.8 (C^{B1}), 129.5 (C^{C3}), 128.2 (C^{B2}), 126.5 (C^{a}), 124.9 (C^{C3}), 123.4 ($\text{C}^{\text{B3/C4}}$), 123.3 ($\text{C}^{\text{B3/C4}}$), 121.9 (C^{A5}), 119.5 (C^{A3}). UV/VIS (CH_2Cl_2 , 1.90×10^{-5} mol dm^{-3}) $\lambda_{\text{max}}/\text{nm}$ 296 ($\epsilon/\text{dm}^3 \text{ mol}^{-1} \text{ cm}^{-1}$ 53560), 389 (97330). ESI: m/z 695.3 [$\text{M} + \text{H}$]⁺ (calc. 695.3), Found: C 85.49, H 5.64, N 7.96; $\text{C}_{50}\text{H}_{38}\text{N}_4 \cdot 0.5\text{H}_2\text{O}$ requires C 85.32, H 5.58, N 7.96.

Ligand 2: method 2

KO^tBu (243 mg, 2.15 mmol) was added to a solution of 4-(*N,N*-diphenylamino)benzaldehyde (520 mg, 1.9 mmol) and 6,6'-bis-(diethylphosphonomethyl)-2,2'-bipyridine (365 mg, 0.80 mmol) in THF (30 cm³). The reaction mixture was stirred for 2 h at room temperature. After addition of water (10 cm³), THF was removed *in vacuo* and the aqueous phase was extracted with CH₂Cl₂ (3 × 30 cm³). The collected organic layers were washed with brine (30 cm³) and water (50 cm³), dried over MgSO₄ and filtered. After evaporation of solvent, precipitation from CH₂Cl₂/pentane resulted in **2** being isolated as an orange-yellow powder (320 mg, 0.46 mmol, 57.5%). Spectroscopic data: see above.

[Cu(1)₂][PF₆]

[Cu(MeCN)₄][PF₆] (37.3 mg, 0.100 mmol) was dissolved in MeCN (2 cm³) and the solution was added to a solution of compound **1** (36.8 mg, 0.200 mmol) in CHCl₃ (5 cm³). The solution immediately became red in colour and was stirred for 30 min. Addition of Et₂O (10 cm³) afforded a red precipitate, which was collected by filtration over Celite. The product was washed with H₂O and Et₂O and removed from the Celite by dissolution in MeCN. Solvent was removed *in vacuo* and [Cu(1)₂][PF₆] was isolated as red crystals (44.6 mg, 77.3%). ¹H NMR (500 MHz, CD₃CN) δ/ppm 8.26 (d, *J* = 8.0 Hz, 2H, H^{A3}), 8.02 (t, *J* = 7.9 Hz, 2H, H^{A4}), 7.50 (d, *J* = 7.7 Hz, 2H, H^{A5}), 2.22 (s, 6H, H^{Me}), ¹³C NMR (126 MHz, CD₃CN) δ/ppm 158.4 (C^{A6}), 152.6 (C^{A2}), 139.2 (C^{A4}), 126.7 (C^{A5}), 120.4 (C^{A3}), 25.2 (C^{Me}). UV/VIS (CH₂Cl₂, 1.84 × 10⁻⁵ mol dm⁻³) λ_{max}/nm 245 (ε/dm³ mol⁻¹ cm⁻¹ 20 300), 257 (18 650), 298 (26 900), 312sh (18 200), 332sh (3100) 453 (3460). Emission (CH₂Cl₂, λ_{ex} = 300 nm) λ_{em} 351 nm; (CH₂Cl₂, λ_{ex} = 454 nm) λ_{em} 520, 687 nm). MALDI-TOF: *m/z* 431.0 [M - PF₆]⁺ (calc. 431.1), 246.5 [M - 1 - PF₆]⁺ (calc. 247.0). Found: C 49.38, H 4.18, N 9.63; C₂₄H₂₄N₄CuPF₆·1/2H₂O requires C 49.19, H 4.30, N 9.56.

[Cu(2)₂][PF₆]

[Cu(MeCN)₄][PF₆] (26.8 mg, 0.0719 mmol) was dissolved in MeCN (2 cm³) and the solution was added to a solution of **2** (100 mg, 0.14 mmol) in CHCl₃ (10 cm³). The solution immediately changed from yellow to orange and was ultra-sonicated for 60 min. The solvents were then removed *in vacuo* and [Cu(2)₂][PF₆] was isolated as an orange powder (92.5 mg, 0.0578 mmol, 80.4%). ¹H NMR (500 MHz, CDCl₃) δ/ppm 7.90 (d, *J* = 7.6, 4H, H^{A3}), 7.85 (t, *J* = 7.8 Hz, 4H, H^{A4}), 7.74 (d, *J* = 7.7 Hz, 4H, H^{A5}), 7.30 (t, *J* = 7.9 Hz, 16H, H^{C3}), 7.12 (d, *J* = 16.3 Hz, 4H, H^b), 7.08 (m, 24H, H^{C2+C4}), 6.79 (d, *J* = 8.6 Hz, 8H, H^{B3}) overlapping with 6.77 (d, *J* = 16.3 Hz, 4H, H^a), 6.67 (d, *J* = 8.6 Hz, 8H, H^{B2}). ¹³C NMR (126 MHz, CDCl₃) δ/ppm 155.5 (C^{A6}), 152.2 (C^{A2}), 148.9 (C^{B4}), 147.1 (C^{C1}), 138.0 (C^{A4}), 135.0 (H^b), 129.6 (C^{C3}), 128.8 (C^{B1}), 127.9 (C^{B2}), 125.1 (C^{C2}), 124.7 (C^a), 123.9 (C^{C4}), 122.4 (C^{A5}), 122.3 (C^{B3}), 119.9 (C^{A3}). UV/VIS (CH₂Cl₂, 1.25 × 10⁻⁶ mol dm⁻³) λ_{max}/nm 299 (ε/dm³ mol⁻¹ cm⁻¹ 185 400), 400 (235 500); (MeCN, 2.32 × 10⁻⁶ mol dm⁻³) λ_{max}/nm 294 (ε/dm³ mol⁻¹ cm⁻¹ 173 000), 390 (207 000). Emission (CH₂Cl₂, λ_{ex} = 300 or 399 nm) λ_{em} 475 nm (see text). ESI: *m/z* 1453.7 [M - PF₆]⁺ (calc. 1452.6), 695.5 [2 + H]⁺ (calc.

695.3). Found: C 73.98, H 4.76, N 7.71; C₁₀₀H₇₆CuF₆N₈P·MeCN·H₂O requires C 73.92, H 4.93, N 7.61.

Crystal structure determinations

Data were collected on a Bruker SMART or KappaAPEX diffractometer, with data reduction, solution and refinement using the programs APEX2,³¹ SIR92³² and CRYSTALS.³³ ORTEP figures were drawn using Ortep-3 for Windows,³⁴ and structures were analysed with the program Mercury v. 2.4.^{35,36}

Ligand 2

C₄₀H₇₀N₂, *M* = 694.88, yellow plate, orthorhombic, space group *Pbca*, *a* = 8.9360(3), *b* = 15.3904(5), *c* = 26.8164(9) Å, *U* = 3688.0(2) Å³, *Z* = 4, *D_c* = 1.251 Mg m⁻³, μ(Mo-K_α) = 0.565 mm⁻¹, *T* = 100 K. Total 35 364 reflections, 3377 unique, *R*_{int} = 0.068. Refinement of 2724 reflections (244 parameters) with *I* > 2σ(*I*) converged at final *R*₁ = 0.0478 (*R*₁ all data = 0.0629), *wR*₂ = 0.0384 (*wR*₂ all data = 0.0554), *gof* = 1.0410.

[Cu(1)₂][PF₆]

C₂₄H₂₄CuF₆N₄P, *M* = 576.99, red block, monoclinic, space group *P2₁/c*, *a* = 12.7104(6), *b* = 21.9632(11), *c* = 8.7001(5) Å, β = 94.692(2)°, *U* = 2420.6(2) Å³, *Z* = 4, *D_c* = 1.583 Mg m⁻³, μ(Mo-K_α) = 1.036 mm⁻¹, *T* = 123 K. Total 35 645 reflections, 8817 unique, *R*_{int} = 0.030. Refinement of 7537 reflections (325 parameters) with *I* > 2σ(*I*) converged at final *R*₁ = 0.0301 (*R*₁ all data = 0.0370), *wR*₂ = 0.0312 (*wR*₂ all data = 0.0450), *gof* = 1.0891.

[Cu(2)₂][PF₆]

C₁₀₀H₇₆CuF₆N₈P, *M* = 1598.28, orange plate, tetragonal, space group *P4/n*, *a* = *b* = 15.1209(2), *c* = 18.2971(4) Å, *U* = 4183.48(12) Å³, *Z* = 2, *D_c* = 1.27 Mg m⁻³, μ(Mo-K_α) = 0.347 mm⁻¹, *T* = 123 K. Total 49 103 reflections, 7090 unique, *R*_{int} = 0.062. Refinement of 3503 reflections (276 parameters) with *I* > 2σ(*I*) converged at final *R*₁ = 0.0494 (*R*₁ all data = 0.0902), *wR*₂ = 0.0524 (*wR*₂ all data = 0.1193), *gof* = 1.0236.

Preparation of solar cells

TiO₂ paste was prepared adapting the procedure of Grätzel and co-workers;³⁷ changes to the published procedure were the use of a porcelain (in place of alumina) mortar, sonicator bath in place of an ultrasonic horn, terpineol (CAS: 8000-41-7) rather than α-terpineol, and the omission of the three roller mill treatment. The FTO glass (Solaronix TCO22-7, 2.2 mm thickness, sheet resistance ≈ 7 Ω square⁻¹) was cleaned by sonicating in acetone, EtOH, Hellmanex® surfactant (2% in water), water and EtOH baths sequentially for 10 min. After treatment in a UV-O₃ system (Model 256-220, Jelight Company Inc), the FTO plates were immersed in aqueous TiCl₄ solution (40 mmol dm⁻³) at 70 °C for 30 min, and washed with H₂O and EtOH. Nanocrystalline TiO₂ electrodes were made by doctor blading the TiO₂ paste onto a conducting glass slide and kept at room temperature for

10 min to allow the paste to mature to minimize surface irregularities. The electrode was then gradually heated under an air flow at 70 °C for 30 min, 135 °C for 5 min, 325 °C for 5 min, 375 °C for 5 min, 450 °C for 15 min, and 500 °C for 15 min. After annealing, the TiO₂ film was treated with 40 mM TiCl₄ solution as described above, rinsed with H₂O and EtOH and sintered at 500 °C for 30 min. After cooling to ≈80 °C, each electrode was immersed in a DMSO solution of anchoring ligand **3**, **4**, **5** or **6** (1 mmol dm⁻³) for 24 h. The colourless slide was removed from the solution, washed with DMSO and EtOH, and dried. The electrode with adsorbed anchoring ligand was immersed in an EtOH solution of [Cu(**1**)₂][PF₆] or a CH₂Cl₂ solution of [Cu(**2**)₂][PF₆] (0.4 mmol dm⁻³) and this was left to stand for 64 h during which time the slide turned orange. The electrode was removed from the solution and was washed with EtOH.

To prepare the counter electrode, a hole was drilled in an FTO glass plate (cleaned and pre-treated as above). The perforated sheet was heated in air for 15 min at 450 °C to remove organic residues and was then washed as described for the working electrode. The Pt catalyst was deposited on the FTO glass by coating with a drop of H₂PtCl₆, 5 mmol dm⁻³ in propan-2-ol and heated to 400 °C for 15 min.

The dye-covered TiO₂ electrode and Pt counter-electrode were assembled using thermoplast hot-melt sealing foil (Solaronix, Meltonix 1170-25 Series, 25 microns thick) by heating while pressing them together. The electrolyte comprised LiI (0.1 mol dm⁻³), I₂ (0.05 mol dm⁻³), 1-methylbenzimidazole (0.5 mol dm⁻³) and 1-butyl-3-methylimidazolium iodide (0.6 mol dm⁻³) in methoxypropionitrile, and was introduced into the cell by vacuum backfilling. The hole on the counter electrode was finally sealed using the hot-melt sealing foil and a cover glass. Measurements were made by irradiating from behind using a light source SolarSim 150 (100 mW cm⁻² = 1 sun). The power of the simulated light was calibrated by using a reference Si photodiode. The standard dye N719 was purchased from Solaronix.

Computational methods

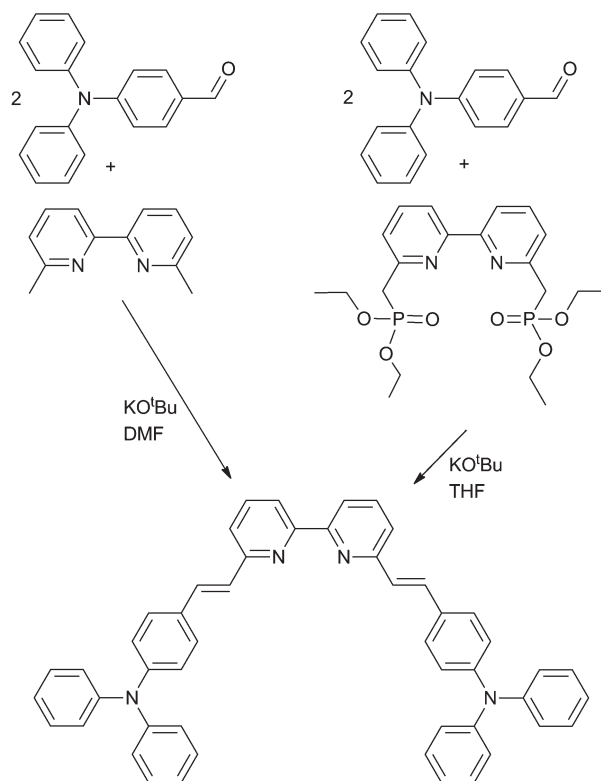
For [CuL₂]⁺ (L = **1** or **2**), the TD-DFT calculations were based upon crystallographic data for a related complex⁶ and [Cu(**2**)₂][PF₆]₂ (this work). For [CuLL']⁺ (L = **1** or **2**, L' = **3–5**) calculations were started from optimized structures of [Cu(**1**)₂]⁺ and [Cu(**2**)₂]⁺ and were computationally modified. Initial energy optimization was carried out at the Hartree–Fock (HF) level with a 3-21G* basis set, followed by HF/6-31G*. Frequency calculations were carried out at this level to confirm that a minimum energy had been achieved. The structures were further relaxed with the hybrid 3-parameter Lee–Yang–Parr functional³⁸ B3LYP/6-31G*. To account for solvent effects, the conductor-like polarizable continuum model (CPCM) was used. The CPCM^{39,40} was used in geometry optimization and for subsequent TD-DFT calculations. As many of the calculations are computationally demanding, the influence of a considerably larger basis set (6-311++G**) was assessed by alternatively using an extended basis set on either the metal atom or on all ligand atoms. This is referred to as GEC and GEL for Gaussian extended basis set on either the copper or the ligand. For the

smaller complexes the entire calculation was also carried out with the 6-311++G** basis set throughout. Explorative calculations were also carried out with a LANL2DZ basis set on the Cu atom⁴¹ and 6-31G* for the remaining system; this is abbreviated as ECP. Predicted electronic transitions were calculated at the B3LYP level and simulated spectra were generated from the Gaussian 09 output using the GaussSum program, version 2.2.⁴² The conversion factor from Hartree to eV is 1 Eh = 27.21128505 eV, taken from the NIST website 2010 values.⁴³ All calculations were carried out using the Gaussian 09 program package.⁴⁴

Results and discussion

Synthesis and characterization of ligand **2**

Compound **2** was prepared by treatment of 6,6'-dimethyl-2,2'-bipyridine (**1**) or 6,6'-bis(diethylphosphonomethyl)-2,2'-bipyridine²⁸ with 4-(*N,N*-diphenylamino)benzaldehyde in the presence of KO^tBu (Scheme 2). Both procedures gave **2** in moderate yields (55–58%). The electrospray mass spectrum of **2** exhibited a peak envelope at *m/z* 695.3 which was assigned to [M + H]⁺. The ¹H and ¹³C NMR spectra were consistent with the symmetrical structure shown in Scheme 1, confirming functionalization in both the 6 and 6'-positions of the 2,2'-bipyridine core. The spectra were assigned using COSY, NOESY, DEPT, HMBC and HMQC methods. Signals for alkene protons H^a and H^b (see Scheme 1) were distinguished by the appearance of H^b/H^{B2} and H^a/H^{A5} cross peaks in the NOESY spectrum; the former cross peak also permitted signals for H^{B2} and H^{B3} to be discriminated.



Scheme 2 Alternative strategies for the synthesis of ligand **2**.

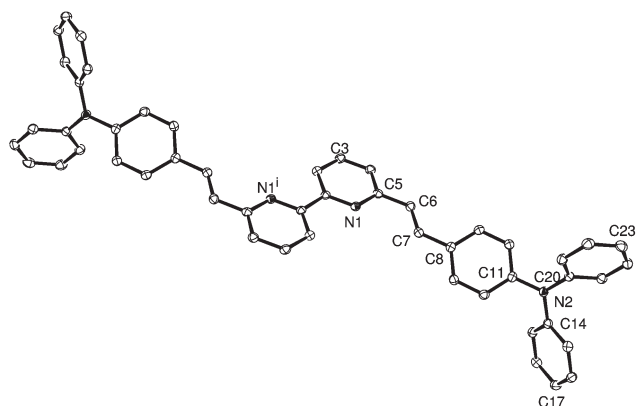


Fig. 1 Molecular structure of compound **2** (ellipsoids plotted at 40% probability level). Important bond parameters: N1–C1 = 1.3424(19), N1–C5 = 1.3515(19), N2–C11 = 1.4247(19), N2–C14 = 1.4181(18), N2–C20 = 1.4175(19), C5–C6 = 1.467(2), C6–C7 = 1.337(2), C7–C8 = 1.461(2) Å; C5–C6–C7 = 123.65(15), C6–C7–C8 = 127.21(14), C11–N2–C14 = 119.28(12), C11–N2–C20 = 119.46(12), C14–N2–C20 = 120.33(12)°. Symmetry code $i = -x, 1 - y, -z$.

The structure of compound **2** was confirmed by single crystal X-ray diffraction, crystals being grown by slow diffusion of hexanes into a CH_2Cl_2 solution of the compound. Fig. 1 depicts the structure of **2**, and selected bond parameters are given in the figure caption. The compound crystallizes in the orthorhombic $Pbca$ space group and the asymmetric unit contains half a molecule, the second half being related to the first by an inversion centre; the bipyridine (bpy) domain is thus necessarily planar. The (*E*)-conformation of the alkene unit is as expected. The C–N–C bond angles around atom N2 (all $\approx 120^\circ$) and the N2–C bond distances (each ≈ 1.42 Å, shorter than the sum of the covalent radii, 1.52 Å) are consistent with sp^2 hybridization and π -contributions to the three N2–C_{arene} bonds. The three aryl substituents adopt a paddle-wheel arrangement around atom N2. The principal packing interactions involve intermeshing of the $\text{Ph}_2\text{NC}_6\text{H}_4$ -units.⁴⁵ This gives rise to domains of $\text{Ph}_2\text{NC}_6\text{H}_4$ -units separated by planar bpy entities (Fig. 2a). Fig. 2b shows a view of the unit cell down the *a*-axis and reveals a herring-bone arrangement of molecules. There are no stacking interactions between bpy units of adjacent molecules.

Synthesis and characterization of copper(i) complexes

Although the $[\text{Cu}(\text{I})_2]^+$ complex cation is well documented in the literature,^{8,19–25} full details of the synthesis and characterization of the hexafluoridophosphate salt have not, to the best of our knowledge, been presented, despite the fact that this salt has appeared in several publications.^{8,24,25} The complex $[\text{Cu}(\text{I})_2][\text{PF}_6]$ was prepared from $[\text{Cu}(\text{MeCN})_4][\text{PF}_6]$ and two equivalents of **1**, and was isolated as a red solid in 77.3% yield. The MALDI-TOF mass spectrum exhibited peak envelopes at m/z 431.0 and 246.5 assigned to the ions $[\text{M} - \text{PF}_6]^+$ and $[\text{M} - \text{I} - \text{PF}_6]^+$. The solution ^1H and ^{13}C NMR spectra were fully assigned (see Experimental section) using 2D NMR techniques. X-ray quality crystals were grown by slow diffusion of Et_2O into an MeCN solution of the complex, and structural analysis confirmed the

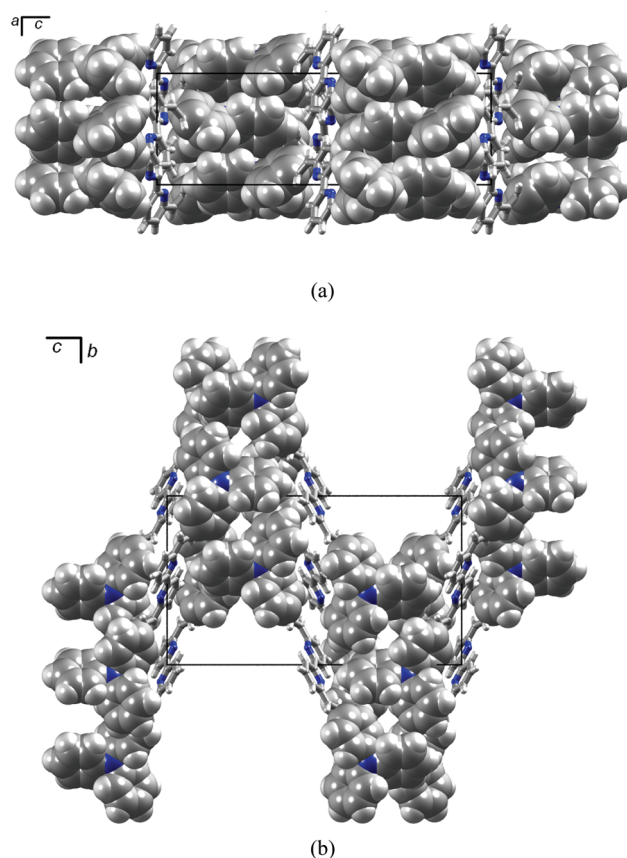


Fig. 2 Packing of molecules of **2** viewed down: (a) the *b*-axis, and (b) the *a*-axis. $\text{Ph}_2\text{NC}_6\text{H}_4$ -units are shown in space-filling representation; N atoms in blue.

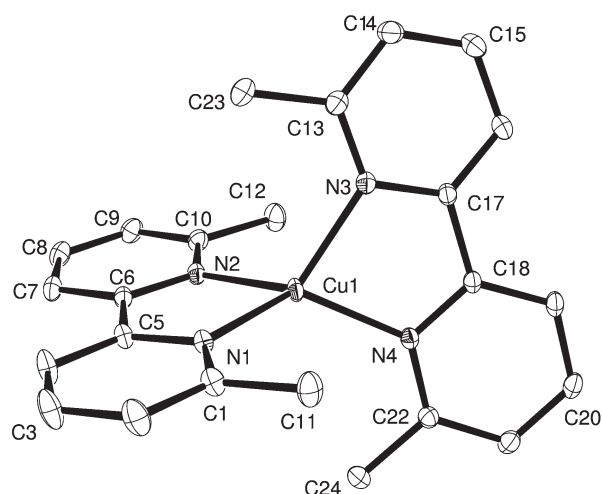


Fig. 3 Structure of the $[\text{Cu}(\text{I})_2]^+$ cation in $[\text{Cu}(\text{I})_2][\text{PF}_6]$ (ellipsoids plotted at 40% probability level). Important bond parameters: Cu1–N1 = 2.0248(9), Cu1–N2 = 2.0472(9), Cu1–N3 = 2.0447(9), Cu1–N4 = 2.0335(9) Å; N1–Cu1–N2 = 81.13(4), N1–Cu1–N3 = 127.51(4), N2–Cu1–N3 = 114.67(4), N1–Cu1–N4 = 125.93(4), N2–Cu1–N4 = 132.08(4), N3–Cu1–N4 = 81.59(3)°.

structure shown in Fig. 3. Selected bond parameters are listed in the caption. The Cu–N bond distances are within the anticipated

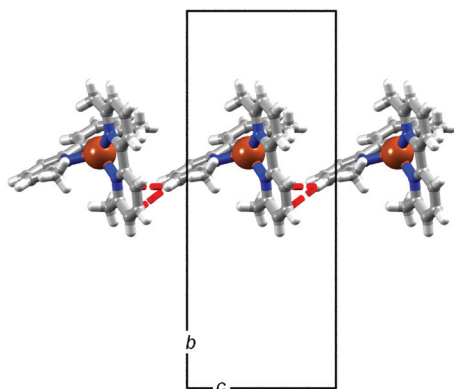


Fig. 4 Assembly of chains of $[\text{Cu}(\mathbf{1})_2]^+$ cations in $[\text{Cu}(\mathbf{1})_2][\text{PF}_6]$ through edge-to-face π -interactions (in red).

range. The copper(i) coordination sphere is flattened tetrahedral, with the angle between the least squares planes containing Cu1 and each bpy unit being $74.33(5)^\circ$. This compares with angles of 80.9° in $[\text{Cu}(\mathbf{1})_2][\text{BF}_4]$ ¹⁹ and 80.7° in $[\text{Cu}(\mathbf{1})_2][\text{ClO}_4]$.²³ This distortion from D_{2d} symmetry in the solid state has been previously discussed and attributed to crystal packing forces.²³ In $[\text{Cu}(\mathbf{1})_2][\text{BF}_4]$ ¹⁹ and $[\text{Cu}(\mathbf{1})_2][\text{ClO}_4]$,²³ the coordinated 6,6'-dimethyl-2,2'-bipyridine ligands are described as being non-planar (twist angles about the 2,2'-carbon-carbon bond of between 2.9 and 13.3° are reported). In $[\text{Cu}(\mathbf{1})_2][\text{PF}_6]$, the angles between the least squares planes of the rings containing N1/N2 and N3/N4 are $0.61(5)$ and $10.65(5)^\circ$, respectively, and we do not consider the deviation from planarity in the latter ligand to be significant. The $[\text{Cu}(\mathbf{1})_2]^+$ cations in $[\text{Cu}(\mathbf{1})_2][\text{PF}_6]$ assemble into chains (running parallel to the c -axis, Fig. 4) supported by edge-to-face π -interactions. The closest contacts are $\text{C14H141}\cdots\text{C7}^i = 2.86 \text{ \AA}$ and $\text{C14H141}\cdots\text{C8}^i = 2.81 \text{ \AA}$ (symmetry code $i = x, y, -1 + z$). Close $\text{CH}\cdots\text{C}_{\text{py}}$ contacts exist between cations in adjacent chains ($\text{C9H91}\cdots\text{C20}^{ii} = 2.87 \text{ \AA}$, symmetry code $ii = 2 - x, 1 - y, 1 - z$), in addition to repulsive $\text{H}\cdots\text{H}$ contacts between methyl groups ($\text{C12H122}\cdots\text{H122}^{ii}\text{C12}^{ii} = 2.35 \text{ \AA}$). These are offset by the extensive $\text{CH}\cdots\text{F}$ interactions throughout the lattice.

The reaction between $[\text{Cu}(\text{MeCN})_4][\text{PF}_6]$ and two equivalents of **2** resulted in the formation of orange $[\text{Cu}(\mathbf{2})_2][\text{PF}_6]$ which was isolated in 80.4% yield. In the electrospray mass spectrum, peaks centred at m/z 1453.7 and 695.5 were assigned to $[\text{M} - \text{PF}_6]^+$ and $[\mathbf{2} + \text{H}]^+$ respectively, and isotope patterns agreed with those simulated. The ^1H and ^{13}C NMR spectra were consistent with the presence of one ligand environment and were assigned using COSY, NOESY, HMQC and HMBC spectra. Both ligand **2** and $[\text{Cu}(\mathbf{2})_2][\text{PF}_6]$ are soluble in CDCl_3 , allowing a direct comparison of the NMR spectra. On going from **2** to $[\text{Cu}(\mathbf{2})_2]^+$, the signal for alkene proton H^b (see Scheme 1) shifts from δ 7.72 to 7.12 ppm, and that for H^a from δ 7.13 to 6.77 ppm. This shielding effect upon complex formation is attributed to the loss of the influence of the nitrogen lone pairs combined with the close proximity of the alkene protons to the copper(i) centre in $[\text{Cu}(\mathbf{2})_2]^+$ (see below). Of the remaining proton signals, that for $\text{H}^{\text{B}2}$ undergoes the most significant perturbation upon ligand coordination, shifting from δ 7.47 to 6.67 ppm. As demonstrated in the structural description below, the two ligands envelop the copper (i) centre, bringing $\text{H}^{\text{B}2}$ within close proximity of the metal ion.

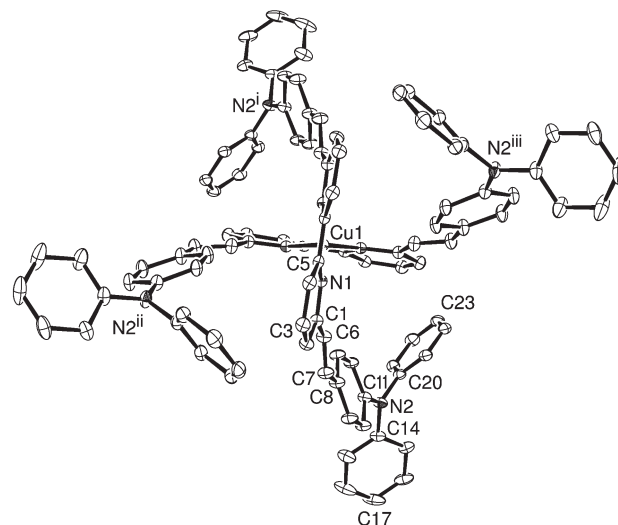


Fig. 5 Structure of the $[\text{Cu}(\mathbf{2})_2]^+$ cation in $[\text{Cu}(\mathbf{2})_2][\text{PF}_6]$ (ellipsoids plotted at 30% probability level). Symmetry codes: $i = 3/2 - x, 1/2 - y, z$; $1 - x, 1/2 + y, -z$; $-1/2 + x, 1 - y, -z$. Important bond parameters: $\text{Cu1-N1} = 2.0379(15)$, $\text{N1-C1} = 1.351(3)$, $\text{C6-C7} = 1.320(3)$, $\text{C7-C8} = 1.465(3)$, $\text{N2-C11} = 1.418(3)$, $\text{N2-C14} = 1.411(3)$, $\text{N2-C20} = 1.426(3) \text{ \AA}$; $\text{N1-Cu1-N1}^i = 80.48(9)$, $\text{N1-Cu1-N1}^{ii} = 125.64(5)$, $\text{C11-N2-C14} = 122.07(18)$, $\text{C11-N2-C20} = 119.02(17)$, $\text{C14-N2-C20} = 118.82(17)^\circ$.

Single crystals of $[\text{Cu}(\mathbf{2})_2][\text{PF}_6]$ were grown by slow diffusion of hexanes into a CH_2Cl_2 solution of the complex, and the structure of the $[\text{Cu}(\mathbf{2})_2]^+$ cation is depicted in Fig. 5. $[\text{Cu}(\mathbf{2})_2][\text{PF}_6]$ crystallizes in the non-chiral tetragonal $P4/n$ space group and residual electron density within the voids in the lattice could not be unambiguously assigned to individual solvent molecules which are severely disordered. The structure was subsequently refined using the program SQUEEZE.⁴⁶ Atom Cu1 lies on a special position $3/4, 1/4, 0$ ($\bar{4}$, cell choice 2, Wyckoff a). The bpy domain is twisted with the angle between the least squares planes of the two pyridine rings being 16.6° . This deformation presumably arises from packing interactions between the two ligands which wrap tightly around the Cu^+ ion, each ligand exhibiting a helical twist (Fig. 6). Both enantiomers of the chiral complex are present in the crystal lattice. In addition to the *trans* to *cis*-conformational change that the bpy domain of ligand **2** undergoes upon coordination, a comparison of the solid-state structures of **2** and $[\text{Cu}(\mathbf{2})_2][\text{PF}_6]$ confirms rotation of the $\text{C}_{\text{pyridine}}-\text{C}_{\text{alkene}}$ bond (C5-C6 in Fig. 1) through $\approx 180^\circ$ (Scheme 3). This enlarges the cavity into which the copper(i) ion is bound. Alkene hydrogen atom H61 (attached to C6, Fig. 5) is only 2.57 \AA away from Cu1. The dominant packing interactions in the lattice involve close $\text{CH}\cdots\text{F}$ contacts and edge-to-face π -interactions involving the pendant phenyl substituents.

Solution photophysical properties of the copper(i) complexes

The electronic absorption spectra of CH_2Cl_2 solutions of ligand **2** and complexes $[\text{Cu}(\mathbf{1})_2][\text{PF}_6]$ and $[\text{Cu}(\mathbf{2})_2][\text{PF}_6]$ are shown in Fig. 7. Each spectrum is dominated by intense, high energy absorptions arising from ligand-based $\pi^* \leftarrow \pi$ transitions. The enhanced intensity of the absorptions on going from $[\text{Cu}(\mathbf{1})_2]$ -

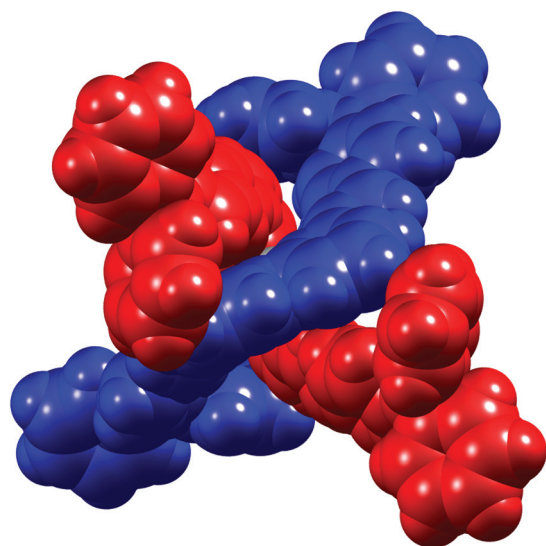
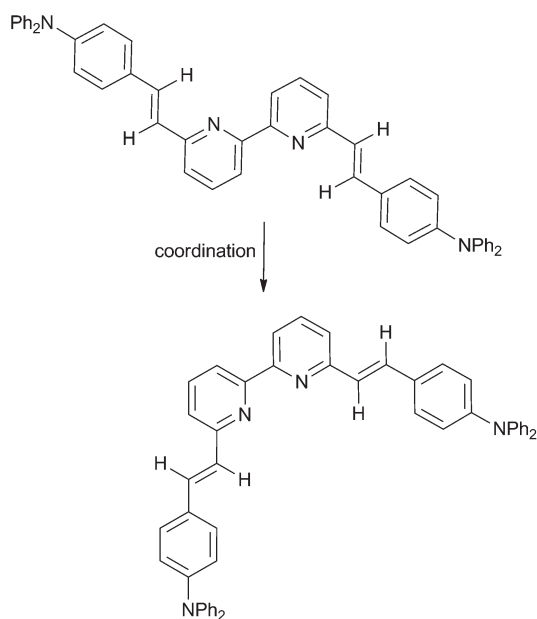


Fig. 6 Space-filling diagram of the $[\text{Cu}(\mathbf{2})_2]^+$ cation in $[\text{Cu}(\mathbf{2})_2][\text{PF}_6]$ with the two ligands shown in red and blue.



Scheme 3 Conformational change of ligand **2** upon binding copper(i).

$[\text{PF}_6]$ to $[\text{Cu}(\mathbf{2})_2][\text{PF}_6]$, and from **2** to $[\text{Cu}(\mathbf{2})][\text{PF}_6]$ is consistent with an increase in the number of aromatic substituents in each case. An MLCT band at 452 nm in the spectrum of $[\text{Cu}(\mathbf{1})_2][\text{PF}_6]$ gives rise to the red colour of the complex, whereas the orange colour of $[\text{Cu}(\mathbf{2})_2][\text{PF}_6]$ is consistent with the tail into the visible of the intense absorption with $\lambda_{\text{max}} = 400$ nm (Fig. 7).

For $[\text{Cu}(\mathbf{1})_2][\text{PF}_6]$, excitation at 300 nm gives rise to an emission at 351 nm, while excitation in the MLCT band ($\lambda_{\text{ex}} = 454$ nm) produces emissions at 520 and 687 nm (lifetimes of 3.98 and 1.95 ns, respectively, with quantum yields $< 0.1\%$). For $[\text{Cu}(\mathbf{2})_2][\text{PF}_6]$, excitation at 300 nm produces a relatively intense emission at 475 nm and weak emission at 340 nm; excitation at 399 nm gives only the emission at 475 nm (lifetime = 2.07 ns,

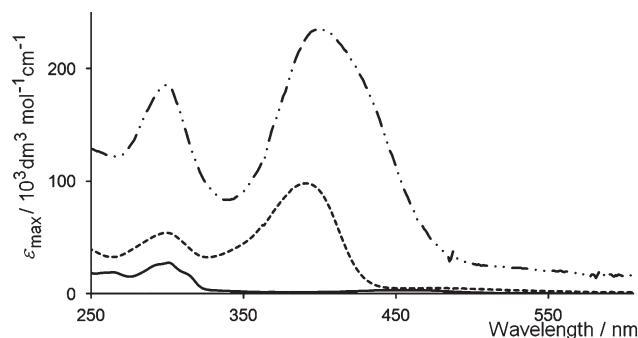


Fig. 7 Electronic absorption spectra of $[\text{Cu}(\mathbf{1})_2][\text{PF}_6]$ (MeCN, —), **2** (CH_2Cl_2 , ---) and $[\text{Cu}(\mathbf{2})_2][\text{PF}_6]$ (CH_2Cl_2 , -·-·-).

Table 1 Redox potentials of ligand **2** and homoleptic copper(i) complexes^a with respect to Fc/Fc^+ (see Experimental section); scan rate of 0.1 V s^{-1} (r = reversible; ir = irreversible; qr = quasi-reversible)

Compound	$E_{1/2}^{\text{ox}}/\text{V}$	$E_{1/2}^{\text{ox}}/\text{V}$	$E_{1/2}^{\text{ox}}/\text{V}$	$E_{1/2}^{\text{red}}/\text{V}$	$E_{1/2}^{\text{red}}/\text{V}$
$[\text{Cu}(\mathbf{1})_2][\text{PF}_6]$			+0.17 ^r	-1.25 ^{qr}	-1.79 ^{ir}
2	+0.65 ^r	+0.47 ^r	+0.43 ^{ir}		
$[\text{Cu}(\mathbf{2})_2][\text{PF}_6]$	+0.50 ^r	+0.32 ^{qr}	—		

^a $[\text{Cu}(\mathbf{1})_2][\text{PF}_6]$ measured in MeCN, **2** and $[\text{Cu}(\mathbf{2})_2][\text{PF}_6]$ measured in CD_2Cl_2 .

quantum yield 37%). The origins of the emissions were confirmed from the excitation spectra.

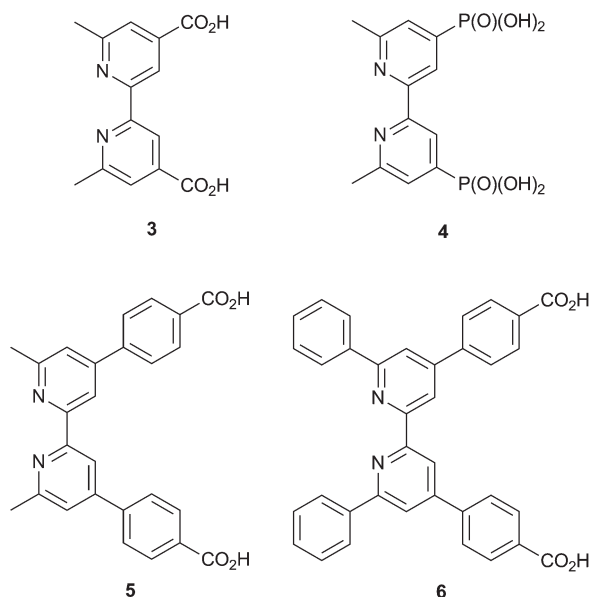
Electrochemical data

Ligand **2** is redox active, exhibiting two reversible and one irreversible oxidation processes. The cyclic voltammogram of $[\text{Cu}(\mathbf{2})_2][\text{PF}_6]$ shows two oxidations which are shifted to lower potential with respect to the reversible processes observed for the free ligand. In contrast, $[\text{Cu}(\mathbf{1})_2][\text{PF}_6]$ exhibits a metal-based oxidation and two ligand-based reductions. The difference in behaviour is consistent with the extended π -conjugation possessed by ligand **2**. Electrochemical data for **2** and the two complexes are summarized in Table 1.

DSCs incorporating heteroleptic copper(i) complexes

Using our recently reported methodology of ligand exchange,¹² a series of eight TiO_2 -bound heteroleptic copper(i) complexes $[\text{CuLL}']^+$ were screened for their efficiency as dyes in DSCs. Ligand L is either **1** or **2**, and L' is one of ligands **3–6** (Scheme 4). The latter contain either carboxylic acid (carboxylate) anchoring groups or phosphonic acid (phosphonate) units. While carboxylate anchoring units are well established in sensitizers, there is evidence that phosphonate groups may lead to higher efficiencies.^{12,47}

We have previously relied upon the use of commercially available titania paste for the construction of solar cells, but have recently begun to prepare TiO_2 pastes using a method adapted from that of Grätzel.³⁷ We have confirmed that its use leads to an enhanced performance of the standard dye N719.



Scheme 4 Structures of the anchoring ligands, 3–6. The anchoring groups are the carboxylic or phosphonic acids or their conjugate bases.

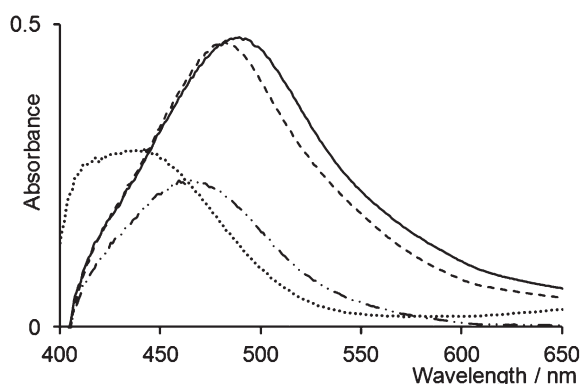


Fig. 8 Solid state electronic absorption spectra of TiO_2 -anchored ligands **3** (.....), **4** (---), **5** (—) and **6** (---) after treatment with $[\text{Cu}(\text{1})_2]^+$ $[\text{PF}_6]^-$.

TiO_2 -anchored heteroleptic $[\text{CuLL}']^+$ complexes were prepared in a step-wise manner. First, the anodes for the solar cells (see Experimental section) were dipped into DMSO solutions of ligands **3**, **4**, **5** or **6**. After washing and drying, the electrodes were immersed in EtOH solutions of $[\text{Cu}(\text{1})_2][\text{PF}_6]$ or CH_2Cl_2 solutions of $[\text{Cu}(\text{2})_2][\text{PF}_6]$ for 64 hours. During this period, the titania changed from colourless to orange. When the slides were washed with EtOH, the orange colour was retained, indicating that ligand exchange at copper(i) had occurred with formation of a surface-bound heteroleptic complex. Fig. 8 shows the UV-VIS spectra of the TiO_2 -bound dyes originating from $[\text{Cu}(\text{1})_2][\text{PF}_6]$. The long tail into the visible region provides support for the presence of surface-bound copper(i) complexes as opposed to free ligands (all are colourless). It is unlikely that the bound species is the homoleptic complex $[\text{Cu}(\text{1})_2]^+$ since ligand **1** has no substituents capable of binding the complex to the surface. The differences in the spectra in Fig. 8 suggest that the surface species are not the homoleptic complexes $[\text{CuL}'_2]^+$ where $L' =$

Table 2 DSC efficiency data compared to standard dye N719 measured under the same conditions. $[\text{Cu}(\text{1})_2]^+$ or $[\text{Cu}(\text{2})_2]^+$ is introduced for surface ligand exchange as the $[\text{PF}_6]^-$ salt

		2 days after sealing of cell			
$[\text{CuL}'_2]^+$	L'	$I_{\text{SC}}/\text{A cm}^{-2}$	V_{OC}/V	ff	$\eta/\%$
$[\text{Cu}(\text{1})_2]^+$	3	0.003	0.518	0.58	1.03
$[\text{Cu}(\text{1})_2]^+$	4	0.004	0.618	0.46	1.18
$[\text{Cu}(\text{1})_2]^+$	5	0.006	0.563	0.45	1.63
$[\text{Cu}(\text{1})_2]^+$	6	0.001	0.536	0.64	0.49
$[\text{Cu}(\text{2})_2]^+$	3	0.001	0.482	0.65	0.47
$[\text{Cu}(\text{2})_2]^+$	4	0.005	0.609	0.60	1.95
$[\text{Cu}(\text{2})_2]^+$	5	0.005	0.555	0.60	1.70
$[\text{Cu}(\text{2})_2]^+$	6	0.001	0.555	0.63	0.51
		7 days after sealing of cell			
$[\text{CuL}'_2]^+$	L'	$I_{\text{SC}}/\text{A cm}^{-2}$	V_{OC}/V	ff	$\eta/\%$
$[\text{Cu}(\text{1})_2]^+$	3	0.004	0.530	0.58	1.17
$[\text{Cu}(\text{1})_2]^+$	4	0.005	0.643	0.44	1.30
$[\text{Cu}(\text{1})_2]^+$	5	0.006	0.595	0.46	1.69
$[\text{Cu}(\text{1})_2]^+$	6	0.001	0.563	0.63	0.45
$[\text{Cu}(\text{2})_2]^+$	3	0.002	0.522	0.66	0.64
$[\text{Cu}(\text{2})_2]^+$	4	0.006	0.627	0.61	2.35
$[\text{Cu}(\text{2})_2]^+$	5	0.007	0.579	0.60	2.33
$[\text{Cu}(\text{2})_2]^+$	6	0.002	0.562	0.63	0.57
N719		0.018	0.718	0.58	7.29

3–6, although we cannot rule out this as a possibility for some of the species present.

Table 2 presents the DSC efficiency data for the solar cells in comparison to those for standard dye N719 measured under the same conditions as the copper(i) complexes. The measurements were made in sealed cells, as opposed to the open cells used previously for copper(i) dyes.¹² Two sets of data are given in Table 2 for each copper-based cell: one 2 days after the cells were sealed, and one 5 days later. For all of the cells, the efficiency was either similar or enhanced over this period. The reason for the improved efficiency is not clear, but formation of aggregates of the sensitizer on the surface probably plays a role.^{48–50}

From the data in Table 2, the best efficiencies are observed by combining ligand **2** with anchoring ligand **4** which contains phosphonate binding groups, and this combination of ligands gives a very promising performance. Relatively good efficiencies are also achieved using anchoring ligand **5**. The superiority of **4** and **5** with respect to **3** and **6** is consistent with our previous observations.¹² For each of anchoring ligands **3**, **4** and **5**, combination with $[\text{Cu}(\text{2})_2]^+$ leads to greater efficiency than with $[\text{Cu}(\text{1})_2]^+$. The poor performance of $[\text{Cu}(\text{2})_2]^+/\text{6}$ may arise from steric crowding at the copper(i) centre caused by the 6- and 6'-phenyl substituents in ligand **6**, leading to low surface coverage of the sensitizer. Comparisons of efficiencies with literature data for other copper(i)-containing DSCs cannot be meaningfully made because of differences in solar cell fabrication, e.g. closed *versus* open cell configuration.

DFT and TD-DFT calculations

The significant effect of the choice of anchoring ligand on the DSC efficiency and the enhancement on going from **1** to **2**

motivated us to investigate the electronic structures of the heteroleptic copper(i) complexes $[\text{Cu}(\text{L})(\text{L}')]^+$ where $\text{L} = \mathbf{1}$ or $\mathbf{2}$, and $\text{L}' = \mathbf{3}$, $\mathbf{4}$ or $\mathbf{5}$. In addition, we have used TD-DFT to predict the electronic absorption spectra of the homo- and heteroleptic complexes. The heteroleptic complexes are difficult to isolate and to study in solution because equilibria are rapidly established involving statistical mixtures of homo- and heteroleptic complexes. The calculations used a polarizable continuum model to take into account the effects of solvent (MeCN). We have chosen to carry out calculations on isolated copper(i) cations. However, the role of the influence of the support has recently been studied for model systems.⁵¹ In our case, the orientation of the copper(i) cations on the TiO_2 surface is not known which makes a meaningful analysis of surface-bound species difficult.

To endorse the DFT geometry optimizations, the calculated geometries within the coordination spheres of $[\text{Cu}(\mathbf{1})_2]^+$ and $[\text{Cu}(\mathbf{2})_2]^+$ were compared with experimental data (this work) for the cations in the hexafluoridophosphate salts (see Table S1†). The agreement between experimentally determined and computed structures supports the choice of the computational method (B3LYP/6-31G*).

A comparison of experimental and theoretical data for each of $[\text{Cu}(\mathbf{1})_2]^+$ and $[\text{Cu}(\mathbf{2})_2]^+$ allows us to assess to what extent TD-DFT calculations correctly describe the electronic absorption spectra of these complexes. Electronic transition data obtained from the TD-DFT calculations for $[\text{Cu}(\mathbf{1})_2]^+$ are shown in Fig. 9 and are compared with the experimental spectrum (for the $[\text{PF}_6]^-$ salt) recorded in MeCN. The choice of basis set was found to be critical. The red and blue curves in Fig. 9b represent the calculated spectra using a 6-31G* and 6-311++G** basis set

on all atoms, respectively. Both basis sets reproduce the ligand-based $\pi^* \leftarrow \pi$ transitions in the UV region of the spectrum rather well. However, the utility of calculations with the smaller basis set (red curve in Fig. 9b) is limited in two respects: (i) contrary to a single MLCT band observed at 452 nm the computations lead to two well defined MLCT bands (see below) in the spectrum at 532 and 378 nm, and (ii) the lowest energy absorption is red-shifted by 80 nm with respect to the observed wavelength. One possible cause for this is the absence of counter-ion in the TD-DFT calculations. We note, however, that similar calculations performed by Lu *et al.*¹⁸ for the related complex $[\text{CuL}_2]^+$ (L is the dimethyl ester of ligand $\mathbf{3}$) illustrate that the inclusion of a $[\text{PF}_6]^-$ counter-ion has little effect on the band shape and λ_{max} . Thus, we do not consider that points (i) and (ii) above originate from the absence of the counter-ion in the calculations. The dominant contributions to the absorption maxima at 532 and 378 nm (red curve in Fig. 9b) involve $\text{LUMO} \leftarrow (\text{HOMO} - 1)$ and $(\text{LUMO} + 1) \leftarrow (\text{HOMO})$ transitions for the lower energy band and $(\text{LUMO} + 2) \leftarrow (\text{HOMO} - 1)$ and $(\text{LUMO} + 3) \leftarrow \text{HOMO}$ transitions for the band at 378 nm. The HOMO and $(\text{HOMO} - 1)$ have predominantly Cu *d*-orbital character with smaller contributions from the bpy domains. The four lowest unoccupied MOs are predominantly ligand-based. Using the considerably larger 6-311++G** basis set (including diffuse functions) results in a blue shift for both MLCT bands. With this larger basis the calculated MLCT maximum shifts to 489 nm (compared to 452 nm from experiment) and the higher energy band at 353 nm merges into the ligand-based bands and corresponds to the shoulder observed experimentally at 332 nm. The characters of corresponding orbitals listed in Table 3 are little altered on changing the basis set.

For the $[\text{Cu}(\mathbf{1})_2]^+$ complex, computations with the 6-311++G** basis set are feasible, while for the considerably larger complexes discussed further below, this is no longer the case. Therefore, the electronic absorption spectrum was computed by using split basis sets GEC and GEL (see Methods).

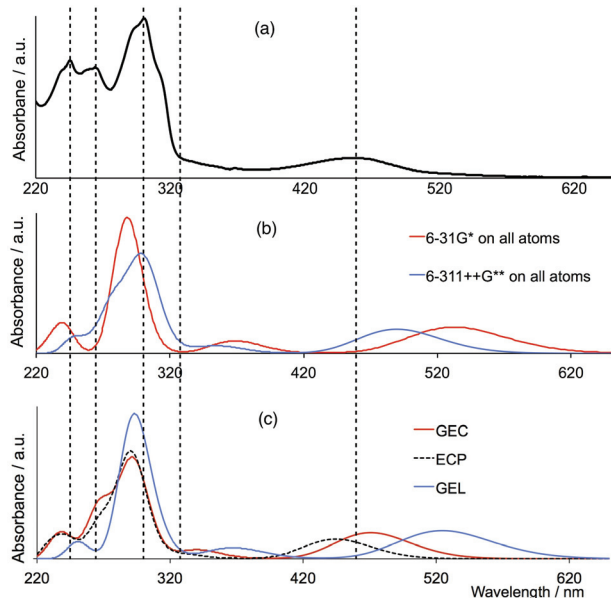


Fig. 9 Electronic absorption spectra of $[\text{Cu}(\mathbf{1})_2]^+$: (a) experimental (MeCN solution), (b) calculated 6-31G* or 6-311++G** on all atoms, (c) split basis sets: red line = GEC; blue line = GEL, black dashed line = ECP. The first 50 transitions were calculated. Dashed vertical lines guide the eye to directly compare experimental and calculated line positions. The figures were generated using the output of the GaussSum program.⁵²

Table 3 Oscillator strengths (f) and orbital contributions to the electronic absorption transitions making up the MLCT band in the visible region for $[\text{Cu}(\mathbf{1})_2]^+$

Basis set	$\lambda_{\text{max}}/\text{nm}$	f	Orbital contributions
6-31G* on all atoms	532	0.22	46% $\text{LUMO} \leftarrow (\text{HOMO} - 1)$ 42% $(\text{LUMO} + 1) \leftarrow (\text{HOMO} - 1)$ 6% $(\text{LUMO} + 1) \leftarrow (\text{HOMO} - 1)$ 6% $\text{LUMO} \leftarrow \text{HOMO}$
6-311++G** on all atoms	489	0.20	46% $\text{LUMO} \leftarrow (\text{HOMO} - 1)$ 40% $(\text{LUMO} + 1) \leftarrow \text{HOMO}$ 7% $(\text{LUMO} + 1) \leftarrow (\text{HOMO} - 1)$ 7% $\text{LUMO} \leftarrow \text{HOMO}$
GEL	524	0.22	46% $\text{LUMO} \leftarrow (\text{HOMO} - 1)$ 42% $(\text{LUMO} + 1) \leftarrow (\text{HOMO} - 1)$ 6% $(\text{LUMO} + 1) \leftarrow (\text{HOMO} - 1)$ 6% $\text{LUMO} \leftarrow \text{HOMO}$
GEC	470	0.20	45% $\text{LUMO} \leftarrow (\text{HOMO} - 1)$ 40% $(\text{LUMO} + 1) \leftarrow \text{HOMO}$ 7% $(\text{LUMO} + 1) \leftarrow (\text{HOMO} - 1)$ 7% $\text{LUMO} \leftarrow \text{HOMO}$

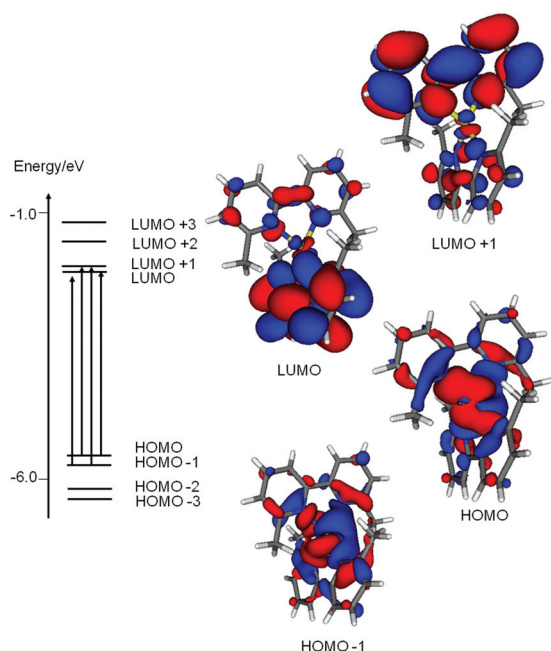


Fig. 10 Diagram illustrating the dominant components of the calculated MLCT band at 470 nm for $[\text{Cu}(\mathbf{1})_2]^+$ (basis set: GEC). Isodensity surfaces for the MOs were generated from the Kohn-Sham orbitals using the MOLEKEL program⁵³ and were plotted at 0.02.

With GEC, the electronic absorption spectrum (red line in Fig. 9c) compares favourably with the experimental spectrum as does that calculated at the 6-311++G** level for all atoms (Fig. 9b). As a control, we also performed the calculation using the GEL basis. This leads to a spectrum (blue line in Fig. 9c) with the deficiencies (i) and (ii) already noted above. However, the ligand-based transitions that give rise to the absorptions in the UV region of the spectrum are adequately predicted. The electronic spectrum with the ECP basis (dashed line in Fig. 9c) is in similarly good agreement with experiment as that with GEC. We conclude that the electronic absorption spectrum of $[\text{Cu}(\mathbf{1})_2]^+$ can be realistically captured using either the GEC or ECP basis set. The transitions using the GEC basis set are represented in the energy level diagram in Fig. 10.

Fig. 11 shows that the single absorption at 390 nm observed experimentally for $[\text{Cu}(\mathbf{2})_2]^+$ ($[\text{PF}_6]^-$ salt in MeCN) is red-shifted to 438 nm by TD-DFT calculations carried out at the 6-31G* level. The predicted spectrum is little different using the GEC basis (Fig. 11). The transitions that make up this band (Table S2 and Fig. S1†) include both MLCT and ligand-based transitions, and contributing orbitals are illustrated in Fig. 12. Of the six highest-lying occupied orbitals involved, two are metal-based (HOMO – 4) and (HOMO – 5)) and four are ligand-centred. The dominance of ligand character in the highest lying occupied MOs in $[\text{Cu}(\mathbf{2})_2]^+$ (HOMO to (HOMO – 3)) is consistent with the observed electrochemical behaviour of this cation described earlier (Table 1).

The above discussion reveals a satisfactory level of confidence in the TD-DFT calculations for homoleptic complexes $[\text{Cu}(\mathbf{1})_2]^+$ and $[\text{Cu}(\mathbf{2})_2]^+$, and we now turn our attention to heteroleptic complexes $[\text{Cu}(\text{L})(\text{L}')]^+$ (L = 1, 2 and L' = 3–5) for which

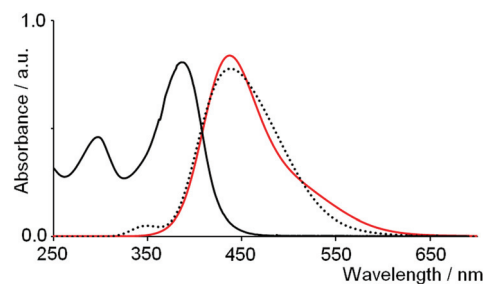


Fig. 11 Electronic absorption spectra of $[\text{Cu}(\mathbf{2})_2]^+$: experimental (black line, MeCN) and calculated (red line = 6-31G* on all atoms, dotted black line = GEC basis). The first 50 transitions were calculated. The figures were generated using the output of the GaussSum program.⁵¹

experimental data are sparse. Previously reported TD-DFT calculations of Lu *et al.* focused particularly on $[\text{CuL}_2]^+$ complexes in which L is a bpy ligand substituted in the 4,4'-positions with CO_2H or CO_2Me anchoring groups.^{17,18} This work confirmed localization of metal and of ligand character in the HOMOs and LUMOs, respectively, of the complexes, a situation that is desirable for electron injection from the anchoring ligand to the semiconductor in a DSC. For all of the TD-DFT calculations on the heteroleptic complexes, the GEC basis was used.

For $[\text{Cu}(\mathbf{1})(\mathbf{3})]^+$, $[\text{Cu}(\mathbf{1})(\mathbf{4})]^+$ and $[\text{Cu}(\mathbf{1})(\mathbf{5})]^+$, the calculations reveal that the HOMOs have dominant metal character (Fig. S1–S3†). In $[\text{Cu}(\mathbf{1})(\mathbf{3})]^+$, the (HOMO – 1) consists of metal and ligand 1 character with a small contribution from the anchoring ligand, and a similar orbital composition is found for the (HOMO – 3) in $[\text{Cu}(\mathbf{1})(\mathbf{4})]^+$ (Fig. S1 and S2†). In $[\text{Cu}(\mathbf{1})(\mathbf{4})]^+$, the LUMO and (LUMO + 2) are localized on anchoring ligand 4 (desirable for electron injection) while the (LUMO + 1) is essentially localized on ligand 1 (Fig. S3†). In $[\text{Cu}(\mathbf{1})(\mathbf{5})]^+$, three of the four lowest lying empty MOs are effectively localized on anchoring ligand 5 (Fig. S4†). For the heteroleptic complexes involving ligand 2, the situation is less well-defined. In each of $[\text{Cu}(\mathbf{2})(\mathbf{3})]^+$ and $[\text{Cu}(\mathbf{2})(\mathbf{4})]^+$, the highest lying occupied MOs are predominantly ligand-based; in $[\text{Cu}(\mathbf{2})(\mathbf{5})]^+$, the HOMO and (HOMO – 1) are ligand-centred while metal character appears in orbitals (HOMO – 2) and those of lower energy. In $[\text{Cu}(\mathbf{2})(\mathbf{3})]^+$, the (LUMO + 2) is essentially localized on anchoring ligand 3, while the LUMO, (LUMO + 1) and (LUMO + 3) are localized on ligand 2; the (LUMO + 4) and (LUMO + 5) possess orbital character from both ligands (Fig. S6†). In $[\text{Cu}(\mathbf{2})(\mathbf{4})]^+$, the LUMO, (LUMO + 4) and (LUMO + 5) are centred on the anchoring phosphonate ligand while the next three lowest lying vacant MOs are localized on ligand 2 (Fig. S7†). In practice, $[\text{Cu}(\mathbf{2})(\mathbf{4})]^+$ is the most efficient dye of those screened (Table 2) and it is pleasing that the TD-DFT data reveal dominant phosphonate ligand character in the LUMO as required for efficient electron injection. The theoretical results may also suggest that the highly conjugated ligand 2 enhances the performance of the DSC by minimizing back-migration of an electron from the semiconductor to the dye (*i.e.* orbital character in the HOMOs is dominated by the non-anchoring ligand). The TD-DFT results show a similar picture for $[\text{Cu}(\mathbf{2})(\mathbf{5})]^+$. Anchoring ligand character is present in the LUMO, (LUMO + 2) and (LUMO + 5)

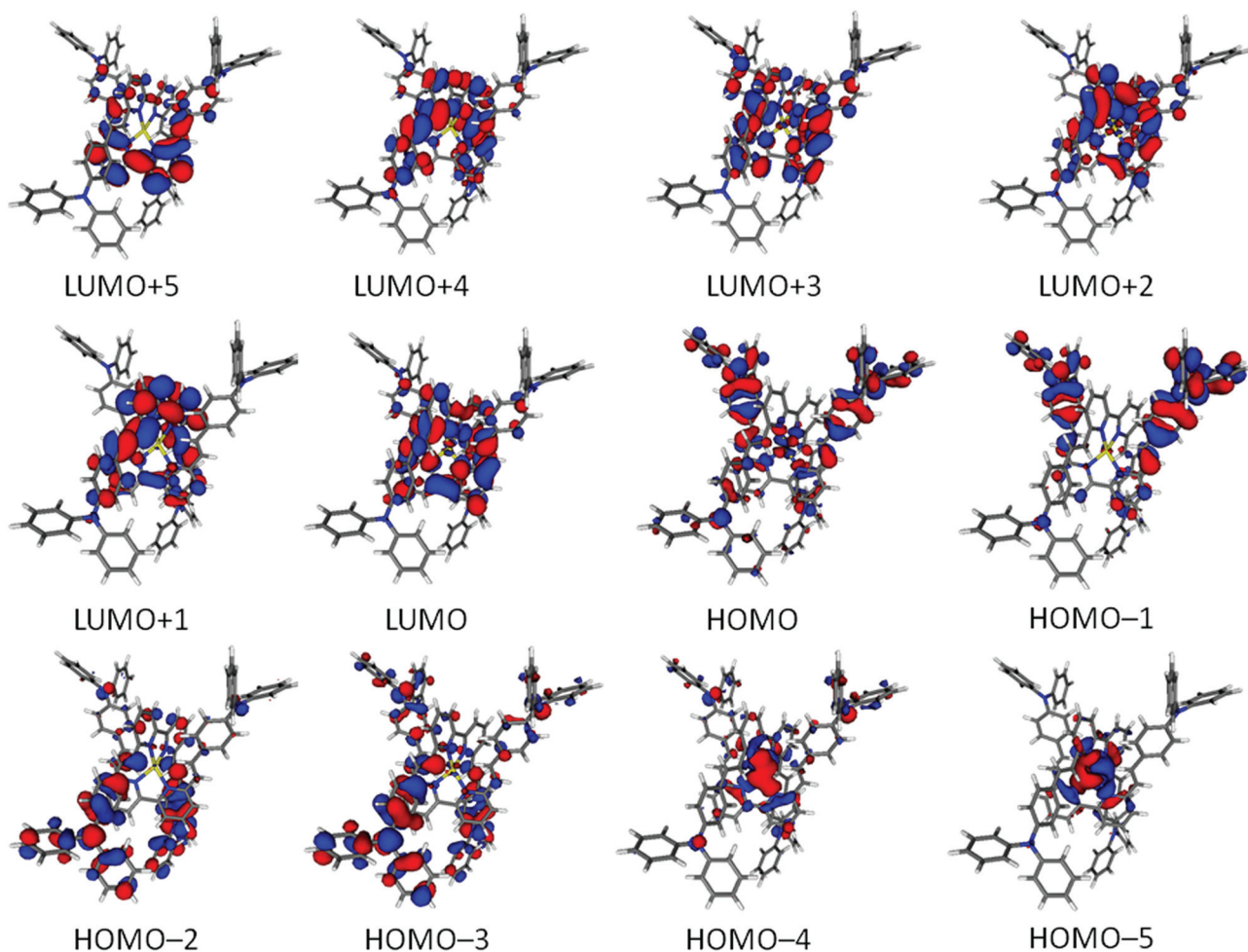


Fig. 12 Molecular orbitals that are the major contributors to the transitions that make up the calculated MLCT band at 380 nm for $[\text{Cu}(\mathbf{2})_2]^+$ with the GEC basis. Isodensity surfaces for the MOs were generated from the Kohn-Sham orbitals using the MOLEKEL program⁵² and were plotted at 0.02.

Table 4 Calculated HOMO–LUMO gaps for $[\text{Cu}(\mathbf{1})(\text{L})]^+$ ($\text{L} = \mathbf{1}, \mathbf{3}, \mathbf{4}, \mathbf{5}$) and $[\text{Cu}(\mathbf{2})(\text{L})]^+$ ($\text{L} = \mathbf{2}, \mathbf{3}, \mathbf{4}, \mathbf{5}$)

Complex	HOMO–LUMO gap/eV	Complex	HOMO–LUMO gap/eV
$[\text{Cu}(\mathbf{1})_2]^+$	3.42	$[\text{Cu}(\mathbf{2})_2]^+$	2.87
$[\text{Cu}(\mathbf{1})(\mathbf{3})]^+$	2.87	$[\text{Cu}(\mathbf{2})(\mathbf{3})]^+$	0.23
$[\text{Cu}(\mathbf{1})(\mathbf{4})]^+$	3.17	$[\text{Cu}(\mathbf{2})(\mathbf{4})]^+$	2.60
$[\text{Cu}(\mathbf{1})(\mathbf{5})]^+$	3.11	$[\text{Cu}(\mathbf{2})(\mathbf{5})]^+$	2.66

(Fig. S8[†]) and ligand **2** character is dominant among the remaining vacant orbitals.

The HOMO–LUMO gaps for the homoleptic and heteroleptic complexes are compared in Table 4. The energy gap is reduced on going from $[\text{Cu}(\mathbf{1})_2]^+$ to $[\text{Cu}(\mathbf{2})_2]^+$, and the same trend is observed between pairs of compounds with a common anchoring ligand. These results serve to emphasize that the electronic absorption spectra of complex molecules of this type are dominated by numerous electronic transitions and not simply by the HOMO–LUMO gap. This is further emphasized by the observation that using the smaller basis set, all HOMO–LUMO gaps are between 2.49 and 3.09 eV and exhibit the same trends as in

Table 4. The detailed origin of the electronic transitions is explored below. At this point we emphasize that the one-electron HOMO–LUMO gap in these complexes is a somewhat artificial guideline due to the cluster of energetically similar frontier orbitals, as exemplified in complex $[\text{Cu}(\mathbf{2})(\mathbf{3})]^+$.

Electronic transition data for the six heteroleptic complexes from the TD-DFT calculations are shown in Fig. 13 and 14. The dominant contributions to the absorption maxima in the calculated spectra of $[\text{Cu}(\mathbf{1})(\text{L})]^+$ ($\text{L} = \mathbf{3}, \mathbf{4}, \mathbf{5}$) are listed in Table 5, and Fig. S1–S3[†] depict the MOs involved in these transitions. For $[\text{Cu}(\mathbf{1})(\mathbf{4})]^+$ and $[\text{Cu}(\mathbf{1})(\mathbf{5})]^+$, metal-to-anchoring ligand transitions make a significant contribution to the absorption bands, whereas for $[\text{Cu}(\mathbf{1})(\mathbf{3})]^+$, the dominance of the LUMO \leftarrow HOMO transition means that the anchoring ligand is little involved. These results are consistent with our observations that the efficiencies of sensitizers $[\text{Cu}(\mathbf{1})(\mathbf{4})]^+$ and $[\text{Cu}(\mathbf{1})(\mathbf{5})]^+$ are greater than that of $[\text{Cu}(\mathbf{1})(\mathbf{3})]^+$ (Table 2).

The calculated absorption spectra for $[\text{Cu}(\mathbf{2})(\text{L})]^+$ ($\text{L} = \mathbf{3}, \mathbf{4}, \mathbf{5}$) (Fig. 14 and S5[†]) are all similar. Just as was seen for $[\text{Cu}(\mathbf{2})_2]^+$, the predicted absorption spectra for the heteroleptic complexes containing **2** are composed of multiple transitions (Table S3[†]) and involve both MLCT and ligand-based transitions. Both filled

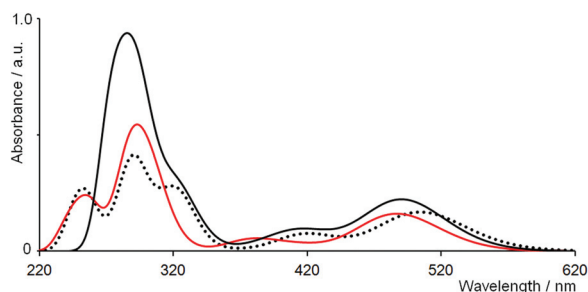


Fig. 13 Calculated electronic absorption spectra of $[\text{Cu}(1)(\text{L}')]^+$ ($\text{L}' = 3-5$): **3** (black line), **4** (red), **5** (dotted). The first 50 transitions were calculated. The figure was produced using the output of the GaussSum program.⁵¹

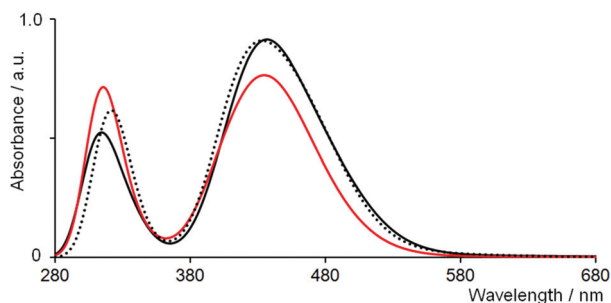


Fig. 14 Calculated electronic absorption spectra of $[\text{Cu}(2)(\text{L}')]^+$ ($\text{L}' = 3-5$): **3** (black line), **4** (red), **5** (dotted). The first 50 transitions were calculated. The figure was generated from the output of the GaussSum program.⁵²

Table 5 Oscillator strengths (f) and orbital contributions to the electronic absorption transitions in the calculated spectra of $[\text{Cu}(1)(\text{L})]^+$ ($\text{L} = 3, 4, 5$)

Complex	$\lambda_{\text{max}}/\text{nm}$	f	Orbital contributions
$[\text{Cu}(1)(3)]^+$	504	0.23	86% LUMO \leftarrow HOMO 12% (LUMO + 1) \leftarrow (HOMO - 1)
	418	0.06	97% (LUMO + 1) \leftarrow HOMO
$[\text{Cu}(1)(4)]^+$	486	0.22	81% LUMO \leftarrow HOMO 15% (LUMO + 1) \leftarrow (HOMO - 1)
	382	0.05	91% (LUMO + 2) \leftarrow HOMO 4% LUMO \leftarrow (HOMO - 3)
$[\text{Cu}(1)(5)]^+$	491	0.31	71% LUMO \leftarrow HOMO 16% (LUMO + 1) \leftarrow (HOMO - 1) 7% LUMO \leftarrow (HOMO - 1)
	414	0.03	3% (LUMO + 3) \leftarrow HOMO 77% (LUMO + 2) \leftarrow HOMO 19% (LUMO + 2) \leftarrow (HOMO - 1)

and vacant MOs involved in the majority of transitions possess some degree of ligand **2** character.

Conclusions

We have performed a combined experimental and TD-DFT computational study on $[\text{Cu}(1)_2]^+$ and $[\text{Cu}(2)_2]^+$ (Scheme 1) to investigate the effects of significantly extending the conjugated π -system in the ligand. We have compared the structures and properties of the homoleptic copper(i) complexes $[\text{Cu}(1)_2][\text{PF}_6]$

and $[\text{Cu}(2)_2][\text{PF}_6]$, and have applied a ligand exchange strategy to prepare eight TiO_2 surface-bound heteroleptic complexes incorporating carboxylate or phosphonate anchoring groups (Scheme 4). Screening of their efficiencies as dyes in DSCs indicates that incorporation of the extended π -conjugation in **2** enhances dye performance with respect to complexes containing ligand **1**, and that combinations of **2** with anchoring ligands **4** (phosphonate anchor) and **5** (phenyl-4-carboxylate anchor) generate the most efficient sensitizers. Of note experimentally are the enhanced intensities of the high-energy bands in the electronic absorption spectrum of $[\text{Cu}(2)_2]^+$ compared to those of $[\text{Cu}(1)_2]^+$ (a consequence of the increased π -system in **2**) and the fact that the cyclic voltammogram of $[\text{Cu}(2)_2][\text{PF}_6]$ shows only ligand-based redox processes in contrast to a well defined copper-centred reversible oxidation and two ligand-based reductions for $[\text{Cu}(1)_2][\text{PF}_6]$. Results of TD-DFT calculations are in accord with these experimental data. They reproduce an electronic absorption spectrum with an MLCT band and high-energy ligand-based transitions for $[\text{Cu}(1)_2]^+$, while predicting a spectrum for $[\text{Cu}(2)_2]^+$, the transitions in which have significant contributions from orbitals with ligand **2** character. For $[\text{Cu}(1)_2]^+$, the calculated electronic absorption spectrum is greatly influenced by the choice of atomic orbital basis set; a 6-31G* basis set on all atoms or mixed GEL basis predicts two MLCT bands at ≈ 530 and 380 nm, while using a 6-311++G** basis set on all atoms or a mixed GEC basis set results in a more realistic calculated spectrum. Using the GEC basis, TD-DFT calculations have been carried out to predict the electronic absorption spectra of the heteroleptic complexes $[\text{Cu}(1)(\text{L})]^+$ and $[\text{Cu}(2)(\text{L})]^+$ ($\text{L} = 3, 4, 5$), and the transitions making up the dominant bands have been analysed in terms of the character of the HOMO–LUMO manifold. For $[\text{Cu}(1)(4)]^+$ and $[\text{Cu}(1)(5)]^+$, metal-to-anchoring ligand transitions contribute significantly to the absorption bands, whereas for $[\text{Cu}(1)(3)]^+$, anchoring ligand **3** is little involved, consistent with the poor performance of $[\text{Cu}(1)(3)]^+$ in the DSCs. Experimental device data indicate that $[\text{Cu}(2)(4)]^+$ is the most efficient dye of those screened, and consistent with this is the fact that the theoretical data reveal dominant phosphonate ligand character in the LUMO as necessitated for efficient electron injection. The orbital character in the HOMOs of $[\text{Cu}(2)(4)]^+$ and $[\text{Cu}(2)(5)]^+$ (the two most efficient dyes) is dominated by the non-anchoring ligand, suggesting that ligand **2** enhances the performance of the sensitizer by minimizing back-migration of an electron from the semiconductor to the dye.

Acknowledgements

We thank the Swiss National Science Foundation, the European Research Council (Advanced Grant 267816 LiLo), the NCCR-MUST (to MM) and the University of Basel for financial support. Dr Iain Wright is acknowledged for assistance with electrochemical measurements. We thank Dr Trixie Wagner (Novartis Institutes for BioMedical Research) for data collection on compound **2**.

Notes and references

- 1 A. Barbieri, G. Accorsi and N. Armaroli, *Chem. Commun.*, 2008, 2185.

- 2 N. Armaroli, G. Accorsi, F. Cardinali and A. Listorti, *Top. Curr. Chem.*, 2007, **280**, 69.
- 3 T. Bessho, E. C. Constable, M. Grätzel, A. Hernandez Redondo, C. E. Housecroft, W. Kylberg, Md. K. Nazeeruddin, M. Neuburger and S. Schaffner, *Chem. Commun.*, 2008, 3717.
- 4 N. Alonso-Vante, V. Ern, P. Chartier, C. O. Dietrich-Buchecker, D. R. McMillin, P. A. Marnot and J.-P. Sauvage, *New J. Chem.*, 1983, 3.
- 5 N. Alonso-Vante, J.-F. Nierengarten and J.-P. Sauvage, *J. Chem. Soc., Dalton Trans.*, 1994, 1649.
- 6 E. C. Constable, A. Hernandez Redondo, C. E. Housecroft, M. Neuburger and S. Schaffner, *Dalton Trans.*, 2009, 6634.
- 7 S. Sakati, T. Kuroki and T. Hamada, *J. Chem. Soc., Dalton Trans.*, 2002, 840.
- 8 A. Hernandez Redondo, E. C. Constable and C. E. Housecroft, *Chimia*, 2009, **63**, 205.
- 9 C. L. Linfoot, P. Richardson, T. E. Hewat, O. Moudam, M. M. Forde, A. Collins, F. White and N. Robertson, *Dalton Trans.*, 2010, **39**, 8945.
- 10 K. H. Kim, T. Okubo, N. Tanaka, N. Mimura, M. Maekawa and T. Kuroda-Sowa, *Chem. Lett.*, 2010, **39**, 792.
- 11 B. Bozic-Weber, E. C. Constable, C. E. Housecroft, M. Neuburger and J. R. Price, *Dalton Trans.*, 2010, **39**, 3585.
- 12 B. Bozic-Weber, E. C. Constable, C. E. Housecroft, P. Kopecky, M. Neuburger and J. A. Zampese, *Dalton Trans.*, 2011, **40**, 12584.
- 13 R. D. Costa, D. Tordera, E. Ortí, H. J. Bolink, J. Schönle, S. Graber, C. E. Housecroft, E. C. Constable and J. A. Zampese, *J. Mater. Chem.*, 2011, **21**, 16108.
- 14 Y.-J. Yuan, Z.-T. Yu, J.-Y. Zhang and Z.-G. Zou, *Dalton Trans.*, 2012, **41**, 9594.
- 15 Y. Jahng, J. Hazelrigg, D. Kimball, E. Riesgo, R. Wu and R. P. Thummel, *Inorg. Chem.*, 1997, **36**, 5390.
- 16 D. V. Scaltrito, D. W. Thompson, J. A. O'Callaghan and G. J. Meyer, *Coord. Chem. Rev.*, 2000, **208**, 243.
- 17 X. Lu, S. Wei, C.-M. L. Wu, S. Li and W. Guo, *J. Phys. Chem. C*, 2011, **115**, 3753.
- 18 X. Lu, C.-M. L. Wu, S. Wei and W. Guo, *J. Phys. Chem. A*, 2010, **114**, 1178.
- 19 P. J. Burke, D. R. McMillin and W. R. Robinson, *Inorg. Chem.*, 1980, **19**, 1211.
- 20 S. Kitagawa, M. Munakata and A. Higashie, *Inorg. Chim. Acta*, 1984, **84**, 79.
- 21 T. Maruyama and T. Yamamoto, *Inorg. Chim. Acta*, 1995, **238**, 9.
- 22 W. L. Parker and G. A. Crosby, *J. Phys. Chem.*, 1989, **93**, 5692.
- 23 S. Itoh, N. Kishikawa, T. Suzuki and H. D. Takagi, *Dalton Trans.*, 2005, 1066.
- 24 L. Allouche, A. Marquis and J.-M. Lehn, *Chem.–Eur. J.*, 2006, **12**, 7520.
- 25 Z. A. Siddique, Y. Yamamoto, T. Ohno and K. Nozaki, *Inorg. Chem.*, 2003, **42**, 6366.
- 26 W. W. Brandt, F. P. Dwyer and E. D. Gyarfás, *Chem. Rev.*, 1954, **545**, 959.
- 27 G. J. Kubas, *Inorg. Synth.*, 1990, **28**, 68.
- 28 V.-M. Mukkala, M. Kwiatkowski, J. Kankare and H. Takalo, *Helv. Chim. Acta*, 1993, **76**, 893.
- 29 V. Penicaud, F. Odobel and B. Bujoli, *Tetrahedron Lett.*, 1998, **39**, 3689.
- 30 A. Hernández Redondo, Ph.D. thesis, University of Basel, 2009.
- 31 *APEX2, version 2 User Manual, M86-E01078*, Bruker Analytical X-ray Systems, Inc., Madison, WI, 2006.
- 32 A. Altomare, G. Cascarano, G. Giacovazzo, A. Guagliardi, M. C. Burla, G. Polidori and M. Camalli, *J. Appl. Crystallogr.*, 1994, **27**, 435.
- 33 P. W. Betteridge, J. R. Carruthers, R. I. Cooper, K. Prout and D. J. Watkin, *J. Appl. Crystallogr.*, 2003, **36**, 1487.
- 34 L. J. Farrugia, *J. Appl. Crystallogr.*, 1997, **30**, 565.
- 35 I. J. Bruno, J. C. Cole, P. R. Edgington, M. K. Kessler, C. F. Macrae, P. McCabe, J. Pearson and R. Taylor, *Acta Crystallogr., Sect. B: Struct. Sci.*, 2002, **58**, 389.
- 36 C. F. Macrae, I. J. Bruno, J. A. Chisholm, P. R. Edgington, P. McCabe, E. Pidcock, L. Rodriguez-Monge, R. Taylor, J. van de Streek and P. A. Wood, *J. Appl. Crystallogr.*, 2008, **41**, 466.
- 37 S. Ito, P. Chen, P. Comte, M. K. Nazeeruddin, P. Liska, P. Péchy and M. Grätzel, *Prog. Photovoltaics: Res. Appl.*, 2007, **15**, 603.
- 38 A. D. Becke, *J. Chem. Phys.*, 1993, **98**, 5648.
- 39 S. Miertus, E. Scrocco and J. Tomasi, *Chem. Phys.*, 1981, **55**, 117.
- 40 M. Cossi, V. Barone, R. Cammi and J. Tomasi, *Chem. Phys. Lett.*, 1996, **255**, 327.
- 41 P. J. Hay and W. R. Wadt, *J. Chem. Phys.*, 1985, **82**, 299.
- 42 N. M. O'Boyle, A. L. Tenderholt and K. M. Langer, *J. Comput. Chem.*, 2008, **29**, 839.
- 43 http://physics.nist.gov/cgi-bin/cuu/Value?threv|search_for=hartree
- 44 M. J. Frisch, G. W. Trucks, H. B. Schlegel, G. E. Scuseria, M. A. Robb, J. R. Cheeseman, G. Scalmani, V. Barone, B. Mennucci, G. A. Petersson, H. Nakatsuji, M. Caricato, H. P. Hratchian, A. F. Izmaylov, J. Bloino, G. Zheng, J. L. Sonnenberg, M. Hada, M. Ehara, K. Toyota, R. Fukuda, J. Hasegawa, M. Ishida, T. Nakajima, Y. Honda, O. Kitao, H. Nakai, T. Vreven, J. A. Montgomery Jr., J. E. Peralta, F. Ogliaro, M. Bearpark, J. J. Heyd, E. Brothers, K. N. Kudin, V. N. Staroverov, R. Kobayashi, J. Normand, K. Raghavachari, A. Rendell, J. C. Burant, S. S. Iyengar, J. Tomasi, M. Cossi, N. Rega, J. M. Millam, M. Klene, X. Li, J. E. Knox, J. B. Cross, V. Bakken, C. Adamo, J. Jaramillo, R. Gomperts, R. E. Startmann, O. Yazyev, A. J. Austin, R. Cammi, C. Pomelli, J. W. Ochterski, R. L. Martin, K. Morokuma, V. G. Zakrzewski, G. A. Voth, P. Salvador, J. J. Dannenberg, J. M. Dapprich, A. D. Daniels, Ö. Farkas, J. B. Foresman, J. V. Ortiz, J. Cioslowski and D. J. Fox, *GAUSSIAN 09 (Revision A.1)*, Gaussian, Inc., Wallingford, CT, 2009.
- 45 I. Dance and M. Scudder, *CrystEngComm*, 2009, **11**, 2233.
- 46 A. L. Spek, *Acta Crystallogr., Sect. D: Biol. Crystallogr.*, 2009, **65**, 148.
- 47 P. Péchy, F. P. Rotzinger, Md. K. Nazeeruddin, O. Kohle, S. M. Zakeeruddin, R. Humphry-Baker and M. Grätzel, *J. Chem. Soc., Chem. Commun.*, 1995, 65.
- 48 B. Wenger, M. Grätzel and J.-E. Moser, *Chimia*, 2005, **59**, 123.
- 49 B. Wenger, M. Grätzel and J.-E. Moser, *J. Am. Chem. Soc.*, 2005, **127**, 12150.
- 50 V. K. Thorsmølle, B. Wenger, J. Teuscher, C. Bauer and J.-E. Moser, *Chimia*, 2007, **61**, 631.
- 51 A. Kovyshin, F. De Angelis and J. Neugebauer, *Phys. Chem. Chem. Phys.*, 2012, **14**, 8608.
- 52 N. M. O'Boyle, A. L. Tenderholt and K. M. Langner, *J. Comput. Chem.*, 2008, **29**, 839.
- 53 U. Varetto, MOLEKEL 5.0.4.8, Swiss National Supercomputing Centre, Manno, Switzerland.